Nano Research

Open Access

Research Article

Boosting the performance of sodium vanadate as cathode of flexible zinc-ion batteries by incorporating MXenes

Guanglei Zhang, Jiacheng Fan, Jilin Gou, Xiaole Zhao, Jingdi Shang, Libo Wang, Yukai Chang, and Aiguo Zhou ✉

Henan International Joint Research Laboratory for High-Performance Light Metallic Materials and Numerical Simulations, School of Materials Science and Engineering, Henan Polytechnic University, Jiaozuo 454003, China

Cite this article: *Nano Research*, **2025**, *18*, 94907786. https://doi.org/10.26599/NR.2025.94907786

ABSTRACT: Herein, we propose an innovative flexible cathode design for zinc-ion batteries (ZIBs) through the strategic integration of sodium vanadate ($NaV_3O_8·1.5H_2O$) with two-dimensional MXene nanosheets (Ti_3C_2 or Mo_2C). The composite architecture leverages MXene's dual advantages of exceptional electrical conductivity and surface hydrophilicity to significantly enhance the electrochemical performance of the vanadate host. The $NaV_3O_8·1.5H_2O$ was synthesized through a reaction between V_2O_5 and NaCl aqueous solution, followed by hybridization with MXene in NaCl solution. When configured into full cells with zinc foil anode and 3 M $Zn(CF_3SO_3)_2$ electrolyte, the optimized composite with 11 wt.% Ti_3C_2 MXene demonstrates remarkable electrochemical enhancement, delivering a specific capacity of 339.6 mAh/g at 1 A/g, a 30.86% improvement over pristine $NaV_3O_8·1.5H_2O$ (259.5 mAh/g). The MXene-modified cathode exhibits extraordinary cycling stability with near 100% capacity retention after 3800 cycles at 3 A/g, outperforming the pure vanadate counterpart that degrades to 103.6 mAh/g after only 2000 cycles. A capacity improvement, the incorporation of MXene also increases the structural stability of the cathode during flexible test cycles. It maintains a capacity of 227.9 mAh/g at 1 A/g under extreme 90° bending/twisting deformations. This synergistic combination of high energy density (381.5 mAh/g at 0.1 A/g), ultralong cycle life, and mechanical endurance positions the MXene-vanadate composite as a promising candidate for next-generation flexible energy storage systems.

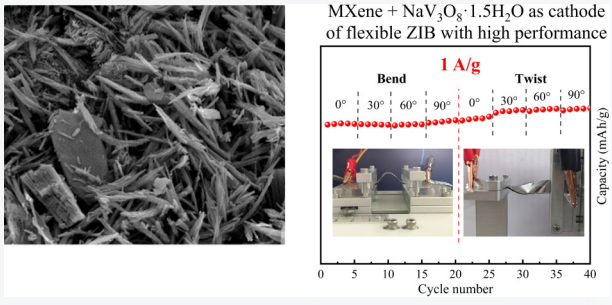

KEYWORDS: MXene, sodium vanadate, zinc-ion batteries

1 Introduction

Zinc-ion batteries (ZIBs) are a promising solution for energy storage in addition to lithium-ion batteries (LIBs) [1, 2]. Compared with lithium in LIBs, zinc has low redox potential (–0.76 V vs. standard hydrogen electrode (SHE)), and zinc metal does not react with water at room temperature [3, 4]. This means that, in ZIBs, zinc metal can be used as anode and aqueous solution can be used as electrolyte, which offers unrivalled safety and an ultra-low environmental impact, compared with LIBs and other types of batteries [5, 6]. Thus, there is a growing interest in the research of aqueous rechargeable ZIBs [7]. However, the cathodes of ZIBs generally have poor electrical conductivity and limited rate capability, which hinder the practical application of aqueous ZIBs [8]. The selection of suitable active material for ZIB cathode is the key to solving these problems. At present, many materials, such as manganese oxides, Prussian blue analogs, and organic compounds, have been investigated [9]. Among those materials, vanadium-based materials, including vanadium oxide, vanadate, and vanadium phosphate [10], are promising due to the multi-valency and low cost of vanadium [11, 12]. Sodium vanadate ($NaV_3O_8·1.5H_2O$ (NVO)) is a type of vanadate that has been explored as cathode material of ZIBs due to its nanobelt morphology and suitable interlayer spacing [13]. However, like other vanadium-based materials, it suffers from poor conductivity and low hydrophilicity [14]. The rate performance and cycling stability are significantly worse than theoretical expectations [15].

To improve the properties of cathode materials, second phases are added to form composites [16]. Two-dimensional (2D) materials, such as graphene [17], MXenes [18, 19], transition metal oxides (TMOs) [20], and transition metal dichalcogenides (TMDs) [21], have been investigated as additive phases to improve the performance of ZIB cathodes, due to their large surface area and

Received: May 12, 2025; **Revised:** July 4, 2025
Accepted: July 10, 2025

✉Address correspondence to zhouag@hpu.edu.cn

open two-dimensional diffusion channels. Among these two-dimensional materials, MXenes have excellent conductivity and hydrophilicity [22]. Combined with their large specific surface area, they can form conductive networks and serve as partial active materials, thereby enhancing conductivity and energy storage performance [23].

MXenes are a family of two-dimensional materials that have been extensively researched in recent years [24–26]. They are derived from MAX phases [27]. The general formula of MXenes is $M_{n+1}X_nT_x$, where M is transition metal (Ti, V, Mo, etc.), X is carbon and/or nitrogen, and T_x presents the surface termination groups (F/OH/O) [28–29]. The typical MXenes are Ti_3C_2 MXene [30] and Mo_2C MXene [31–32]. Similar to graphene (the first 2D material), MXenes have high electrical conductivity and a very large number of active sites [33–34]. Better than graphene, MXenes are hydrophilic. Additionally, Zn^{2+} can rapidly intercalate and deintercalate the interlayer space of MXenes. Thus, it is feasible to apply MXenes as cathodes of aqueous ZIBs [35–36]. However, if used alone, MXenes often lack a clear voltage plateau, resulting in poor discharge performance [4]. As a result, MXenes are mainly employed as additive materials or substrates to enhance the performance of other materials as cathodes [37–38].

In this study, the performance of $NaV_3O_8{\cdot}1.5H_2O$ as cathode of ZIBs was boosted by incorporating MXenes. A composite of NVO and MXene (NVO/MXene) was fabricated and applied as cathodes of ZIBs. In the composite, NVO provides high capacity, MXene enhances the conductivity and hydrophilicity of NVO, and provides some capacity. The composite exhibits excellent rate performance and cycling stability as cathodes of ZIBs, compared with pure sodium vanadate and pure MXene.

To understand the impacts of the type of MXenes, two types of MXenes (Ti_3C_2 MXene and Mo_2C MXene) are selected for this study. The composites of NVO with Ti_3C_2 MXene or Mo_2C MXene were prepared by solution blending. The performances of those composites (MXene/NVO) as cathode of ZIB were investigated. Among the composites, the samples with 11% Ti_3C_2 MXene exhibit the best performance with high capacity (388 mAh/g at 0.1 A/g), excellent rate capability (210.5 mAh/g at 10 A/g), and long-term cycling stability (retaining nearly 100% capacity after 3800 cycles). Moreover, it exhibited excellent performance as flexible cathode. It maintained a stable specific capacity of 227.9 mAh/g (1 A/g) during bending and twisting. Therefore, the composite of $NaV_3O_8{\cdot}1.5H_2O$ incorporated with Ti_3C_2 MXene demonstrates tremendous potential as cathode of flexible ZIBs.

2 Experiment

2.1 Synthesis of Ti_3C_2 MXene and Mo_2C MXene

Ti_3C_2 MXene was prepared from Ti_3AlC_2 prepared by the etching of HCl + NaF solution [30, 39–40]. 2 g NaF (98%, Luoyang Chemical Reagent Factory, China) was dissolved in 6 M HCl solution (12 M, Yantai Shuangshuang Chemical Company, China) to make the etching solution. 2 g of Ti_3AlC_2 powders made in our laboratory [39] were immersed in HCl + NaF solution and stirred at 60 °C for 48 h. Then black powders were separated from the solution and washed repeatedly with deionized water for several times until the pH value reached about 6. Then the powders were vacuum dried at 60 °C for 12 h to obtain Ti_3C_2 MXene.

Mo_2C MXene was made by hydrothermal etching in hydrofluoric acid solution [41–42]. 1 g of precursor Mo_2Ga_2C powders made in our laboratory [43] were slowly added to 40 mL etching solution of HF (40%, Shanghai Macklin, China). Thereafter, the solution was put in an autoclave and kept at 180 °C for 24 h. Then black powders were separated from the solution and washed repeatedly with deionized water for several times until the pH value reached about 6. Then the powders were vacuum dried at 60 °C for 12 h to obtain Mo_2C MXene.

2.2 Synthesis of sodium vanadate nanowires

1 g of V_2O_5 powders (99%, Shanghai Aladdin, China) were added to 15 mL solution of sodium chloride (NaCl, 98%, Luoyang Chemical Reagent, China) with the concentration of 2 M and stirred at 30 °C for 72 h. Dark red powders were separated from the solution and repeatedly washed with deionized water until the chloride ions in centrifuged supernatant could not be tested by silver nitrate solution. The product was then vacuum-dried at 60 °C for 12 h to obtain nanowires of NVO. The reaction followed this equation

$$3V_2O_5 + 2NaCl + 4H_2O \rightarrow 2NaV_3O_8 \cdot 1.5H_2O + 2HCl \quad (1)$$

2.3 Preparation of MXene/NVO cathode materials

Because NVO was slightly soluble in pure water but was not soluble in water with Na^+, NVO and MXene were mixed in NaCl water solution, instead of pure water. The powders of MXene (Ti_3C_2 MXene or Mo_2C MXene, 0.1 g) were added into NaCl solution (15 mL, 2 M) and sonicated for 10 min, then NVO nanowires were added and sonicated for 10 min. The mass percentages of Ti_3C_2 MXene in the composites were 8%, 9%, 11%, 14%, 20%, and 33%, respectively. The corresponding samples were labeled as TNVO8, TNVO9, TNVO11, TNVO14, TNVO20, and TNVO33, respectively. Similarly, the mass percentages of Mo_2C MXene were 3%, 6%, and 11%, respectively. The corresponding samples were labeled as MNVO3, MNVO6, and MNVO11, respectively. Thereafter, the mixtures were stirred for 12 h. Powders were collected from the mixtures by centrifugation. The powders were washed repeatedly with deionized water until no precipitate was detected in the supernatant by silver nitrate solution. The precipitate was generated due to the reaction between residual Cl^- and silver nitrate. Finally, the precipitates were vacuum-dried at 60 °C for 12 h to obtain the MXene/NVO composites.

The dried MXene/NVO (0.14 g) was mixed with acetylene black (0.04 g) and ground for 1 h in an onyx mortar with a pestle. Then the ground mixtures were put into solution of polyvinylidene fluoride (PVDF, 99.7%, Changshu Xinhua Chemical, China). The PVDF solution was made by dissolving 0.02 g PVDF into 300 mL of N-methyl pyrrolidone (NMP, 99.95%, Shanghai Aladdin, China). The PVDF solutions with MXene/NVO (MXene/NVO:acetylene black:PVDF = 7:2:1) were magnetic stirred for 3 h to make uniform slurries.

2.4 Fabrication of ZIBs

Two types of ZIBs were assembled in this paper. The first type was CR2032 coin batteries for energy storage tests without flexible cycles. The second type was quasi-solid-state batteries for the test under flexible cycles.

2.4.1 CR2032 coin batteries

The CR2032 coin batteries were assembled in air with 0.05 mm

thick zinc foil as anodes, 3 M zinc trifluoromethanesulfonic ($Zn(CF_3SO_3)_2$) acid solution as electrolyte, and glass fiber filter paper (Whatman, GF/D, China) as separators. The cathodes were MXene/NVO slices, which were made from the MXene/NVO slurries in Section 2.3. The slurries were coated on glass plate and dried under vacuum at 80 °C for 12 h. After drying, the glass plates were put into deionized water. After 15 min in water, MXene/NVO films were taken off the glass plates and dried at 30 °C in a blast drying oven for 30 min. Thereafter, cathode slices in disc shape with diameter of 14 mm were cut from the films. The mass of each slice was 1.5–2 mg. The thickness was 0.1 mm. The assembly followed the order: anode shell–spring–gasket–zinc foil–separator–cathode slice–cathode shell.

2.4.2 Quasi-solid-state batteries

The anodes of the batteries were zinc foils in rectangular shape (thickness = 0.05 mm, length = 5 cm, and width = 1 cm). The cathodes were MXene/NVO films in same shape with thickness of 0.1 mm, which were fabricated by coating the slurry in Section 2.3 onto a 0.02 mm thick stainless-steel foil, followed by drying and cutting. The electrolyte of the ZIBs was a type of hydrogel. The hydrogel solution was prepared by mixing 15 mL of 3 M zinc trifluoromethanesulfonic acid ($Zn(CF_3SO_3)_2$) solution, 3.3 g of acrylamide (AM, 99.0%, Shanghai Aladdin, China), 0.0013 g of N,N-methylenebisacrylamide (MBA, 99.0%, Shanghai Aladdin, China), and 0.04 g of ammonium persulfate ($(NH_4)_2S_2O_8$, 98%, Tianjin Kemio, China). The solutions were stirred at room temperature for 1 h. The anode and cathode were assembled in a specialized mold. Then the hydrogel solution was poured into the space between anode and cathode with the thickness of 1.5 mm. Finally, the assembled quasi-solid-state batteries were placed flat on a heating platform and cured at 70 °C for 1.5 h to complete the fabrication of the quasi-solid-state battery.

2.5 Material characterization

Compositional analysis was performed by an X-ray diffractometer (XRD, Rigaku, SmartLab, Tokyo, Japan) employing Cu K_α radiation, λ = 1.5406 Å. Morphological and microstructural studies were performed by scanning electron microscope (SEM, Merlin, Compact, Carl Zeiss NTS Ltd., Jena, Germany) equipped with energy-dispersive spectrometer (EDS, X-MaxN, Oxford, UK). The surface chemical state was analyzed by X-ray photoelectron spectroscopy (XPS, ESCALAB 250Xi, Thermo Scientific, USA) using a focused monochromatized Al K_α X-ray source at 1486.5 eV, with the binding energy based on the C 1s peak at 284.6 eV. The contact angle of the cathode sheet to the electrolyte was measured by a contact angle meter (JC2000D1, Shanghai Zhongchen Digital Technology Equipment Co., Ltd., China).

2.6 Electrochemical testing

Electrochemical tests were performed using a battery tester (CT200A, Wuhan Blue Power Electronics, China) with a voltage range of 0.25–1.6 V. Multiplicative discharge performance was tested at current densities of 0.1–10 A/g, and long-cycle discharge performance was tested at current densities of 3 A/g. Cyclic voltammetry (CV) and electrical impedance spectroscopy (EIS) tests were carried out on a CHI660E workstation (Shanghai Chenhua, China) to detect reduction and oxidation peaks in the voltage range of 0.25–1.6 V at a scanning rate of 0.2 mV/s. EIS spectra were examined at a potential amplitude of 5.0 mV and frequencies of 50 mHz and 100 kHz.

3 Results and discussion

3.1 Microstructure characterization

The XRD patterns of Ti_3C_2 MXene, Mo_2C MXene, and their precursors are shown in Fig. 1(a). As shown in Fig. 1(a), all the peaks of precursors disappear in the patterns of Ti_3C_2 MXene and Mo_2C MXene. There are only the peaks of corresponding MXene. Therefore, highly pure Ti_3C_2 MXene and Mo_2C MXene were successfully synthesized. The XRD patterns of NVO and its precursor are shown in Fig. 1(b). All peaks of V_2O_5 disappear in the pattern of NVO. There are only the diffraction peaks of NVO. This indicates the successful synthesis of highly pure NVO. The XRD patterns of MXene/NVO composites are shown in Figs. 1(c) and 1(d). Besides the peak of NVO, the (002) peaks of MXene were observed in the samples with ≥ 14% Ti_3C_2 MXene or ≥ 6% Mo_2C MXene. It is noticed that the (002) peak of Mo_2C MXene is much stronger than that of Ti_3C_2 MXene, even though the ratio of MXene in the composites is same. This is because Mo_2C MXene can keep the multilayer structure better in the composites than Ti_3C_2 MXene.

The SEM images of Ti_3C_2 MXene and Mo_2C MXene are shown in Figs. 2(a) and 2(b), respectively. Both Ti_3C_2 MXene and Mo_2C MXene have multilayer structure. However, the multilayer structure of Ti_3C_2 MXene is loose while that of Mo_2C MXene is compact. These are typical microstructures of Ti_3C_2 MXene [30] and Mo_2C MXene [44]. The SEM images of V_2O_5 and NVO are shown in Figs. 2(c) and 2(d). V_2O_5 are aggregates of particles, and NVO are one-dimensional nanowires. In following Section 3.2, the composites with 11% Ti_3C_2 MXene (TNVO11) and the composites with 6% Mo_2C MXene (MNVO6) exhibit the best electrochemical performance in the corresponding composite series. Thus, the SEM images of the two composites are shown in Figs. 2(e) and 2(f). The atomic percentages obtained by EDS mapping are shown in the insets. As shown in Figs. 2(e) and 2(f), the sheets or multilayer structures of MXene are distributed in the nanowires of NVO. It is clearly demonstrated that the two MXenes have been successfully incorporated with NVO, while each material maintains its distinct morphology.

The XPS spectra of TNVO11 and MNVO6 are shown in Figs. 3(a) and 3(b). The high-resolution XPS spectra are shown in Figs. 3(c)–3(f). Both composites share similar high-resolution spectra for Na 1s and V 2p of NVO, as displayed in Figs. 3(c) and 3(d). The high-resolution Na 1s spectra (Fig. 3(c)) show a single prominent peak around 1071.3 eV, corresponding to the Na element in NVO. The high-resolution V 2p spectra (Fig. 3(d)) reveal two distinct peaks near 525 and 517 eV, resulting from spin-orbit splitting of V 2p into V $2p_{1/2}$ (524.4 eV) and V $2p_{3/2}$ (517.3 eV). This splitting indicates a well-defined dual-phase structure with a mixed valence state of V^{4+} and V^{5+}. The high-resolution Ti 2p spectrum of the composite (Fig. 3(e)) exhibits typical peaks of Ti_3C_2 MXene [45]. Similarly, the high-resolution Mo 3d spectrum (Fig. 3(f)) shows typical peaks corresponding to Mo 3d in Mo_2C MXene [46].

From the XRD, SEM, and XPS results, it can be concluded that the composites of MXene/NVO were successfully prepared. The nanosheets of MXene are encapsulated by the nanowire of NVO.

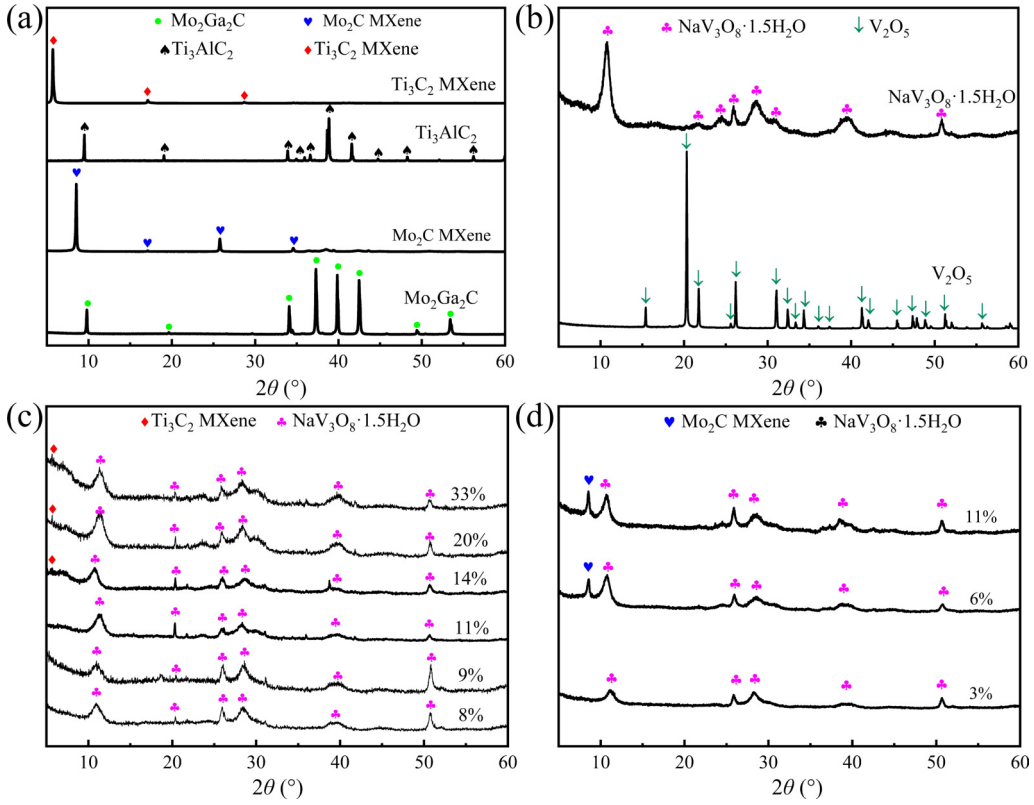

Figure 1 (a) XRD patterns of MXenes and their precursor. (b) XRD patterns of NVO and V_2O_5. (c) XRD patterns of Ti_3C_2 MXene/NVO. (d) XRD patterns of Mo_2C MXene/NVO.

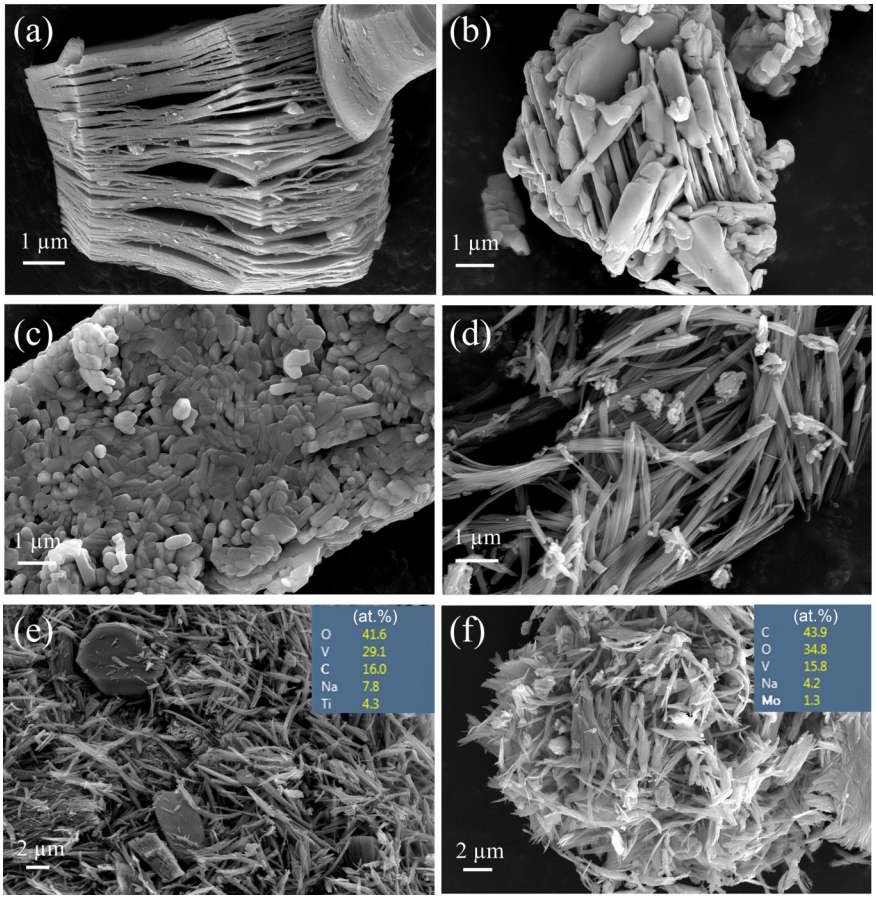

Figure 2 ((a) and (b)) SEM images of Ti_3C_2 MXene and Mo_2C MXene. ((c) and (d)) SEM images of V_2O_5 and $NaV_3O_8{\cdot}1.5H_2O$. (e) SEM image of TNVO11. (f) SEM image of MNVO6.

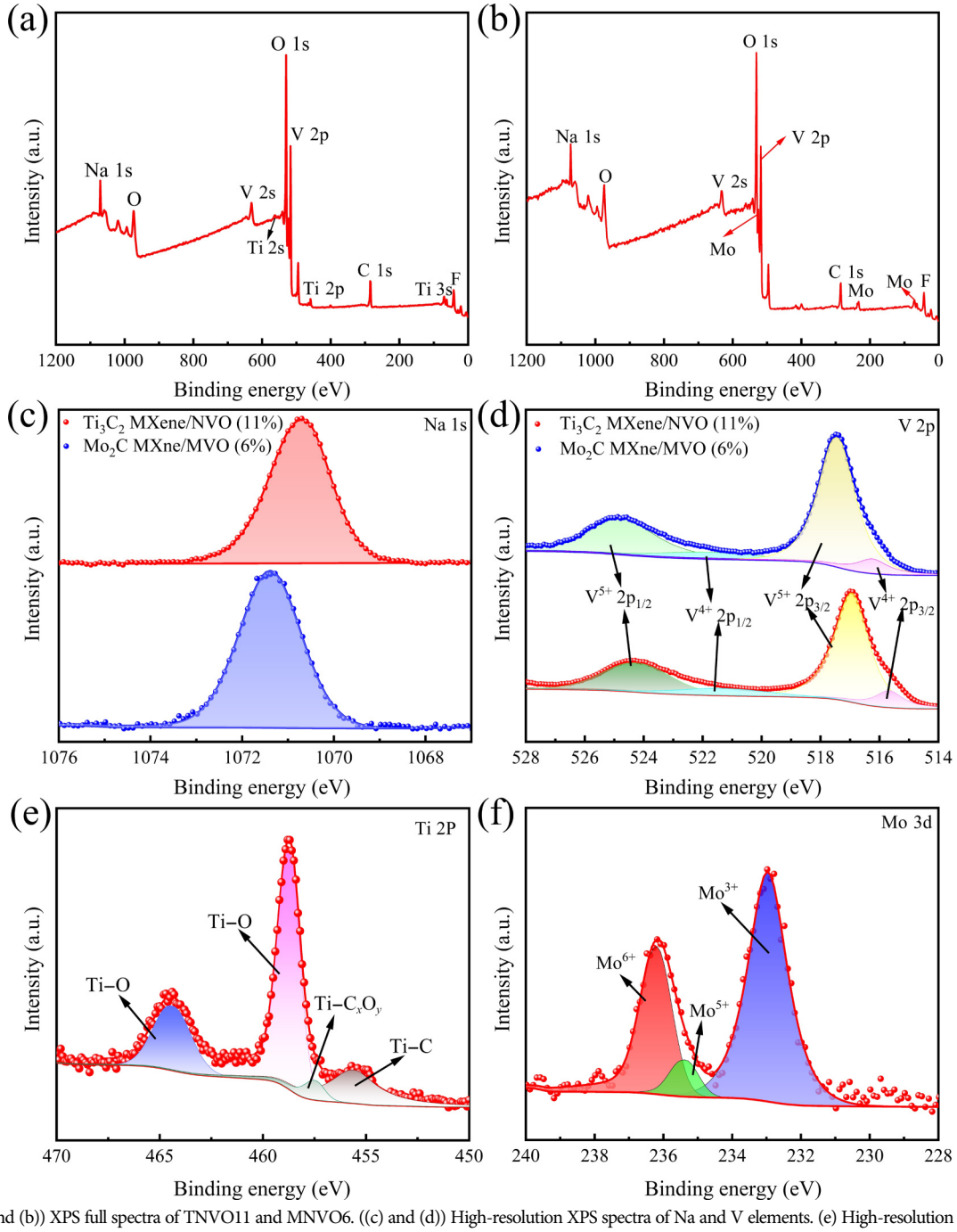

Figure 3 ((a) and (b)) XPS full spectra of TNVO11 and MNVO6. ((c) and (d)) High-resolution XPS spectra of Na and V elements. (e) High-resolution XPS spectrum of Ti in TNVO11. (f) High-resolution XPS spectrum of Mo in MNVO6.

3.2 Electrochemical properties

3.2.1 Energy storage performance of CR2032 coin batteries

The electrochemical performances of MXene/NVO composites are shown in Fig. 4. As shown in Fig. 4(a), if the percentage of Ti_3C_2 MXene < 11%, the performance is enhanced with the increase of Ti_3C_2 MXene percentage. If the percentage > 11%, the performance decreased with the increase of MXene percentage. TNVO11 exhibits the best performance with significantly higher discharge capacity and better cycling stability, compared with pure NVO (Fig. 4(a)). The TNVO11 cathode delivers a high specific capacity of 392.1 mAh/g at a current density of 0.1 A/g. Moreover, it exhibits minimal capacity loss during charge–discharge cycling at varying rates from 0.1 to 1 A/g. At 1 A/g, the specific capacity of TNVO11 was 339.6 mAh/g, while the capacity of pure NVO was 259.5 mAh/g. The incorporation of 11% Ti_3C_2 MXene enhances 30.86% capacity of NVO. Therefore, the addition of Ti_3C_2 MXene with suitable ratio can boost the performance of NVO as ZIB cathodes.

Besides Ti_3C_2 MXene, the effect of the other MXene, Mo_2C MXene, is shown in Fig. 4(b). The addition of Mo_2C MXene can also increase the performance. However, only the composite with the percentage of 6% had enhanced performance. The composites with other percentages had worse performance. The performance

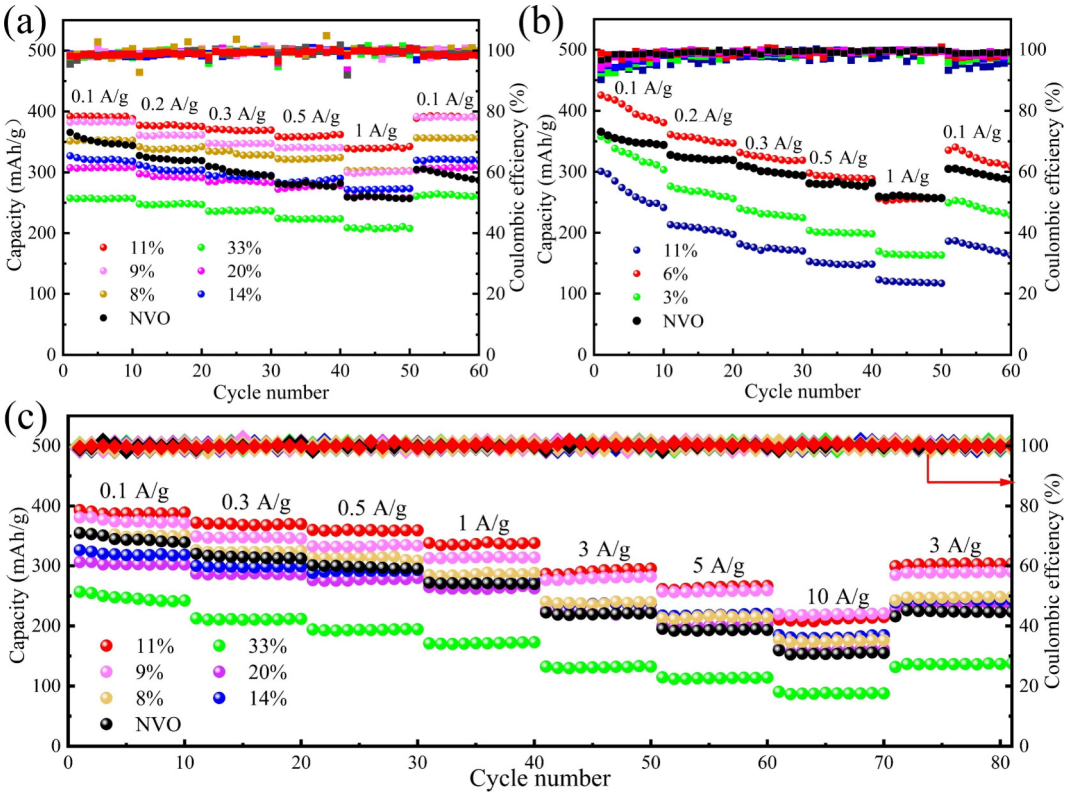

Figure 4 ((a) and (b)) Rate performance curves of NVO with different proportions of Ti_3C_2 MXene and Mo_2C MXene. (c) Rate performance of sodium vanadate with varying Ti_3C_2 MXene contents under high current densities.

of MNVO6 was worse than that of TNVO11. Therefore, Ti_3C_2 MXene is a better additive than Mo_2C MXene to enhance the performance of NVO. The following sections of this paper focus exclusively on the electrochemical performance of the Ti_3C_2 MXene/NVO composite. The high-rate performance of composite electrodes with different ratios of Ti_3C_2 MXene/NVO is shown in Fig. 4(c). The TNVO11 electrode exhibits significantly higher zinc storage capacity and excellent rate performance compared to the NVO electrode. At a current density of 10 A/g, it retains a specific capacity of 212.1 mAh/g, with only a 46.3% decrease in capacity even if the current density is increased by 100 times, which is quite impressive.

As observed in Figs. 4(a) and 4(c), TNVO11 consistently demonstrates the optimal composite ratio, exhibiting superior rate performance both at low and high current densities. Therefore, further investigations will focus solely on this composition.

The data collected from the first three cycles of cyclic voltammetry tests, conducted at a scan rate of 0.2 mV/s and a voltage window of 0.25–1.6 V, are shown in Fig. 5(a). Two distinct pairs of redox peaks are clearly observed. During the initial charge–discharge cycle, a deviation in the redox peak positions is noted due to the absence of Zn^{2+} in the cathode material, which results in discrepancies compared to the peaks observed in the second and third cycles. After the first charge–discharge cycle, Zn^{2+} is successfully embedded into the composite material, and the two pairs of redox peaks stabilize at 0.55/0.77 and 0.85/1.06 V. These two pairs of redox reactions can be described as the transition from $NaZn_{0.1}V_3O_8{\cdot}1.5H_2O$ to $H_{2.14}NaZn_{0.2}V_3O_8{\cdot}1.5H_2O$, and further to $H_{3.9}NaZn_{0.5}V_3O_8{\cdot}1.5H_2O$ [13]. In this process, the oxidation state of vanadium (V) changes from V^{5+} to V^{4+}, and from V^{4+} to V^{3+}. At a current density of 0.1 A/g, the charge–discharge capacity–voltage curves of the TNVO11 electrode during the first three cycles are presented in Fig. 5(b). These curves are consistent with the CV results shown in Fig. 5(a), exhibiting distinct voltage plateaus at the corresponding redox potentials. Moreover, the charge–discharge curves exhibit significant overlap after the first cycle, indicating excellent cycling stability of the TNVO electrode. Moreover, the TNVO11 electrode exhibits excellent cycling stability, maintaining a high specific capacity of 297.5 mAh/g and a nearly 100% Coulombic efficiency after over 3800 cycles at a high current density of 3 A/g (Fig. 5(c)). In contrast, the NVO electrode shows a specific capacity of only 103.6 mAh/g after 2000 cycles at the same current density.

To investigate the mechanism behind the exceptional zinc storage performance of the TNVO11 cathode, its contact angle with the electrolyte (3 M $Zn(CF_3SO_3)_2$) was measured and shown in Fig. 6. The contact angle of TNVO11 with the electrolyte was 72.4°, compared to 83.0° for NVO alone. This indicates that the incorporation of Ti_3C_2 MXene enhances the affinity of NVO for the electrolyte.

To further investigate the mechanism behind the superior zinc storage performance of the TNVO11, CV tests were conducted at varying scan rates of 0.2, 0.4, 0.6, 0.8, and 1 mV/s (Fig. 7(a)). Two distinct pairs of redox peaks are observed within the voltage range of 0.25–1.6 V. The relationship between the current (i) and the peak scan rate for each redox peak can be expressed using Eqs. (2) and (3), where i and v are the peak current and scan rate, and a and b are variables that can be used to determine pseudo-capacitance behavior. The slope value (b-value) is commonly used to distinguish different electrochemical processes [47]

$$i = av^b \tag{2}$$

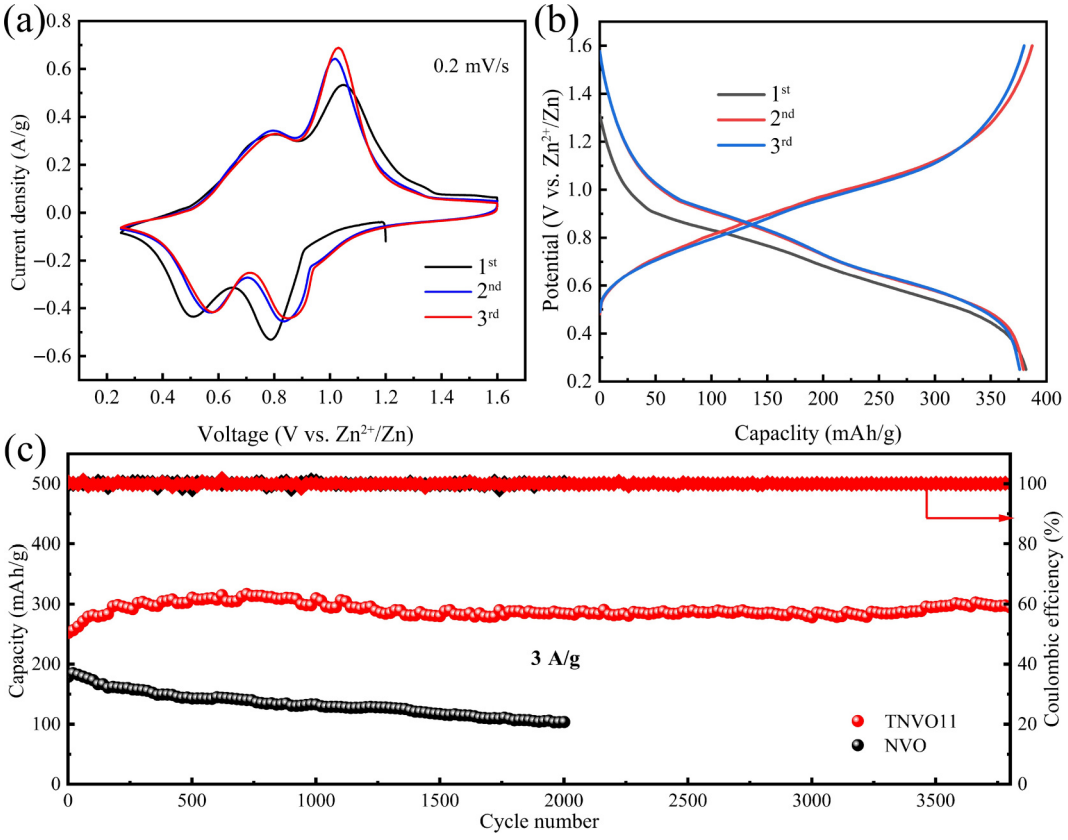

Figure 5 (a) The first three charge–discharge CV curves of TNVO11 at a scan rate of 0.2 mV/s. (b) The voltage–capacity curves of the TNVO11 electrode during the first three charge–discharge cycles at a current density of 0.1 A/g. (c) Comparison of the long-cycling performance of NVO and TNVO11 at high current densities of 3 A/g.

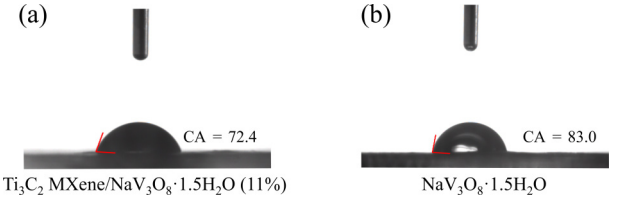

Figure 6 (a) Contact angle of TNVO11 with the electrolyte. (b) Contact angle of NVO with the electrolyte.

$$\log(i) = b\log(v) + \log(a) \tag{3}$$

The calculated b-values for TNVO11 are 0.93, 0.57, 0.87, and 0.65 (Fig. 7(b)), indicating that the electrochemical reaction is primarily governed by pseudocapacitive behavior. Additionally, the capacitive contribution at different scan rates can be calculated using Eq. (4) [48]

$$i = k_1 v + k_2 v^{0.5} \text{ or } i/v^{0.5} = k_1 v^{0.5} + k_2 \tag{4}$$

where k_1 and k_2 are constants. The calculation results are shown in Fig. 7(c), where the capacitive contribution increases with the scan rate. At a low scan rate of 0.2 mV/s, the capacitive contribution reaches as high as 57% (Fig. 7(d)), indicating that the composite electrode exhibits favorable ion transport kinetics, with fast ion diffusion and transfer rates.

In order to further investigate the reason for the fast ion diffusion rate, we use the electrochemical impedance test and galvanostatic intermittent titration technique (GITT) to study the diffusion kinetics of ions. The electrochemical impedance spectroscopy (EIS) plots of the TNVO11 and NVO are shown in Fig. 8(a), with the circuit model used for fitting. The radius of the semicircular portion of TNVO11 is significantly smaller than that of NVO. Therefore, the incorporation of Ti_3C_2 MXene in NVO can improve conductivity and increase ion diffusion rate. The results of GITT are shown in Fig. 8(b). The test was conducted at a current density of 0.1 A/g, with charging or discharging for 10 min, followed by a 40 min rest period to allow the electrode to reach thermodynamic stability, as shown in Fig. 8(c). Based on the results in Fig. 8(c), the ion migration rate was calculated according to Eq. (5) [15]

$$D = \frac{4L^2}{\pi\tau}\left(\frac{\Delta E_s}{\Delta E_t}\right)^2 \tag{5}$$

The parameters are defined as follows: D denotes the migration rate of Zn^{2+}, τ denotes the relaxation time (s), ΔE_s represents the steady-state voltage change during an individual GITT step, ΔE_t signifies the potential change after internal resistance drop (iR drop) elimination, and L corresponds to the Zn^{2+} diffusion length, which equals the electrode thickness.

The Zn^{2+} ion migration rate ($D_{Zn^{2+}}$) during charging and discharging is found to be $D_{Zn^{2+}} = 3.21 \times 10^{-10}$–$2.29 \times 10^{-9}$ cm²/s, which is higher than those of currently common vanadium-based material composites, 7.32×10^{-12} to 3.14×10^{-10} cm²/s [49–50]. This high ion migration rate is a key factor contributing to the excellent rate performance and stability of the electrode [51].

In summary, the electrochemical performance of the NVO cathode material is significantly enhanced by the incorporation of Ti_3C_2 MXene. The zinc storage mechanism of the TNVO composite material can be attributed to the following aspects:

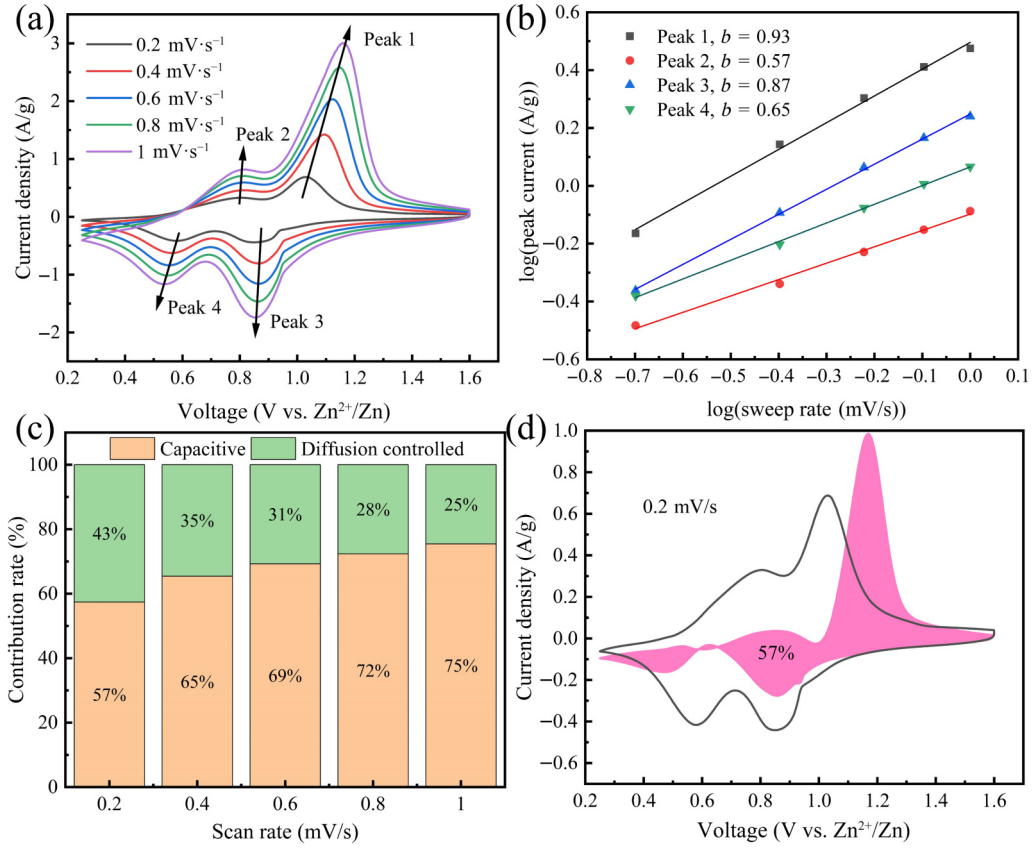

Figure 7 Electrochemical performance of the TNVO11 electrode. (a) CV curves at different scan rates (0.2, 0.4, 0.6, 0.8, and 1 mV/s). (b) Peak currents log(*i*) and log(*v*). (c) Ratio of pseudocapacitance contribution at different scan rates. (d) Pseudocapacitance curves at a scan rate of 0.2 mV/s.

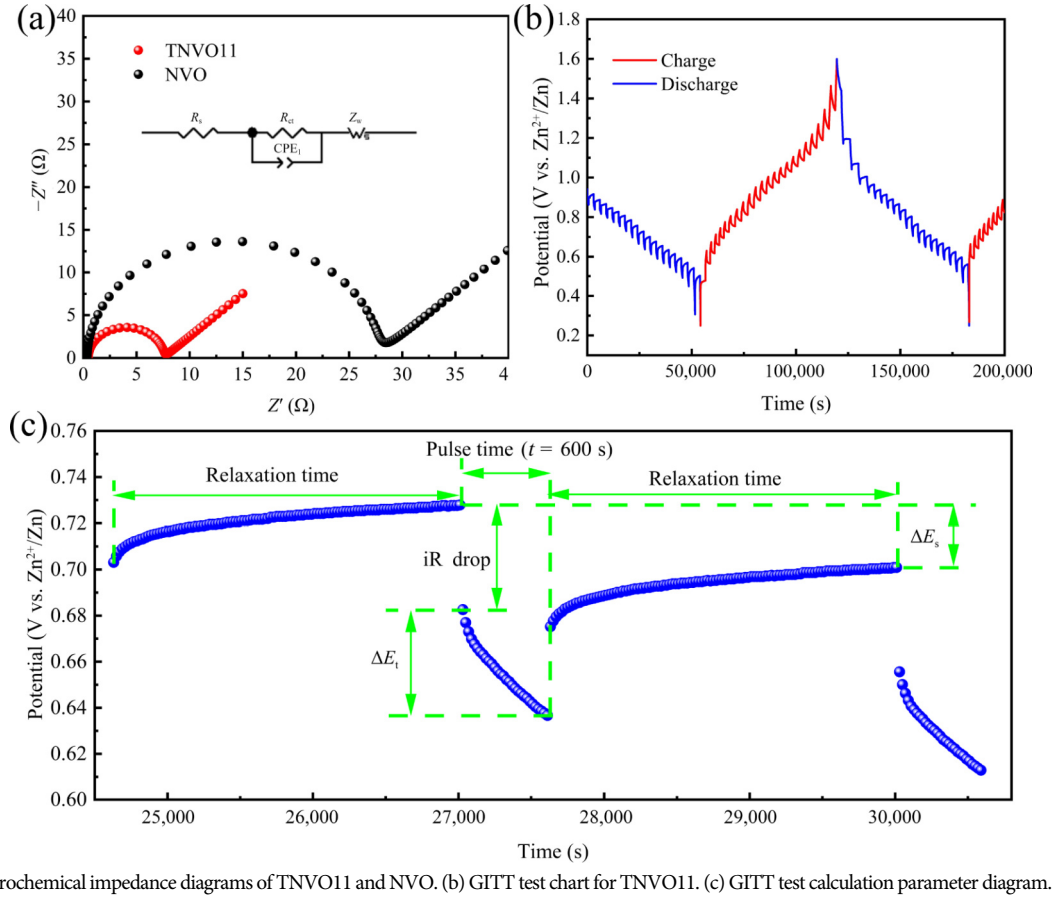

Figure 8 (a) Electrochemical impedance diagrams of TNVO11 and NVO. (b) GITT test chart for TNVO11. (c) GITT test calculation parameter diagram.

(1) The primary energy storage mechanism of the TNVO composite material is the redox reaction of NVO. However, since Ti_3C_2 MXene also possesses a layered structure with interlayer active sites, it can contribute partially to the overall energy storage.

(2) The main role of Ti_3C_2 MXene in the composite electrode is to provide high electrical conductivity and mitigate the volume changes induced by the repeated insertion/extraction of Zn^{2+} in NVO. This effectively reduces structural degradation and enhances cycling stability.

(3) The high conductivity and hydrophilicity of Ti_3C_2 MXene significantly accelerate electron transport within the electrode, facilitating faster surface electrochemical reactions on NVO. Consequently, the rate capability of the composite electrode is greatly improved.

3.2.2 *Flexible quasi-solid-state batteries*

A key feature of aqueous zinc-ion batteries is that they can maintain high energy storage performance during flexible cycles. Therefore, in this study, a quasi-solid-state battery with TNVO11 as cathode was fabricated. The rate performance is shown in Fig. 9(a). Even at high current densities of 0.1, 0.3, 0.5, 1, and 3 A/g, the zinc-ion battery still maintains a high specific capacity of 320.7, 274.6, 243.5, 227.9, and 150.7 mAh/g, respectively. To evaluate the zinc storage performance during flexible cycles, charge–discharge tests were conducted at a current density of 1 A/g while subjected to bending (Fig. 9(b)) and twisting (Fig. 9(c)). The results, shown in Fig. 9(d), clearly demonstrate that the specific capacity remains highly stable under both bending and twisting conditions, with even a slight upward trend, which is quite impressive. This remarkable zinc storage capability can be attributed to the excellent ion transport properties and exceptional structural stability of the TNVO11 composite electrode, which demonstrates tremendous potential for flexible, wearable applications.

The performance of TNVO11 was compared with that of other ZIB cathodes in Table 1. As shown in the table, the TNVO11 electrode demonstrates superior zinc storage capacity and outstanding rate performance. If the current density was increased by a factor of 40, the NVO electrode retained only 44% of its capacity, 165 mAh/g at 4 A/g [13]. In contrast, even if the current density was increased by a factor of 100, TNVO11 retains 54.6% of its capacity, 212.1 mAh/g at 10 A/g. Compared with other cathodes enhanced with MXene listed in Table 1, the rate performance of TNVO11 studied in this paper is the highest. Furthermore, TNVO11 material is also suitable for flexible energy storage applications, a feature that many aqueous zinc-ion cathode materials cannot match. As shown in Table 1, TNVO11 exhibits a capacity of 320.7 mAh/g at a current density of 0.1 A/g for flexible batteries, significantly outperforming other electrode materials in terms of zinc storage at the same current density. Additionally, it is noteworthy that there are very few reports on the twisting performance of flexible batteries in the current literature. However, the flexible battery fabricated with TNVO11 as the cathode material is able to easily achieve a 90° twist while maintaining stable output at a current density of 1 A/g.

4 Conclusion

The performance of $NaV_3O_8{\cdot}1.5H_2O$ as cathode of ZIB can be remarkably enhanced by the incorporation of two-dimensional MXene. Compared with Mo_2C MXene, Ti_3C_2 MXene exhibits better effects. The incorporation of Ti_3C_2 MXene enhanced the ion diffusion rate, electrical conductivity, and hydrophilicity of $NaV_3O_8{\cdot}1.5H_2O$, resulting in high specific capacity, excellent rate performance, and outstanding cycling stability in conventional coin batteries. The $NaV_3O_8{\cdot}1.5H_2O$ composites with 11% Ti_3C_2 MXene (TNVO11) made by a solution blending method exhibited a high

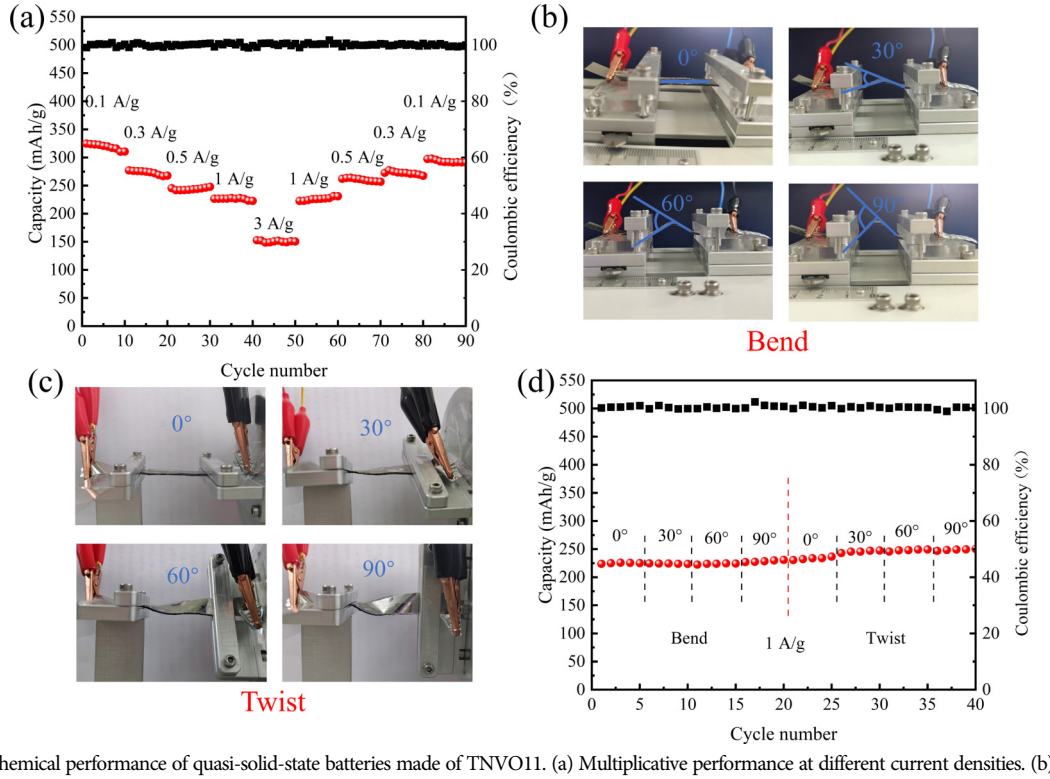

Figure 9 Electrochemical performance of quasi-solid-state batteries made of TNVO11. (a) Multiplicative performance at different current densities. (b) Flexible batteries bending test. (c) Flexible batteries twisting test. (d) Flexible batteries bending and twisting test results.

Table 1 TNVO11 vs. other ZIBs electrodes (in the table, all MXene refers to Ti_3C_2 MXene)

Electrode	Specific capacity	Cycling stability	Capacity of flexible battery	References
MXene/ $NaV_3O_8{\cdot}1.5H_2O$	388.0 mAh/g at 0.1 A/g, 212.1 mAh/g at 10 A/g	= 100% capacity retention after 3700 cycles at 3.0 A/g	320.7 mAh/g at 0.1 A/g	This work
$NaV_3O_8{\cdot}1.5H_2O$	380 mAh/g at 0.1 A/g, 165.0 mAh/g at 4 A/g	82% capacity retention after 1000 cycles at 4.0 A/g	—	[13]
δ-MnO_2/MXene	315 mAh/g at 0.2 A/g, 149 mAh/g at 5 A/g	88.1% capacity retention after 5000 cycles at 5.0 A/g	—	[52]
$Mg_{0.2}V_2O_5{\cdot}nH_2O$	344.0 mAh/g at 0.1 A/g, 218.0 mAh/g at 10 A/g	83.7% capacity retention after 10,000 cycles at 5.0 A/g	309 mAh/g at 0.1 A/g	[53]
$H_2V_3O_8$/MXene	365.3 mAh/g at 0.2 A/g, 163 mAh/g at 10 A/g	= 84% capacity retention after 5600 cycles at 5.0 A/g	252.6 mAh/g at 1 A/g	[11]
VO_2/MXene	363.6 mAh/g at 0.06 A/g, 169.1 mAh/g at 15 A/g	76.0% capacity retention after 5000 cycles at 6.0 A/g	—	[54]
$VO(CH_2O)_2$/ MXene	359.8 mAh/g at 0.5 A/g, 128.1 mAh/g at 10 A/g	85.2% capacity retention after 3000 cycles at 10 A/g	—	[47]
VSe_2/MXene	125.0 mAh/g at 0.1 A/g, 100.0 mAh/g at 5.0 A/g	66.0% capacity retention after 5000 cycles at 5.0 A/g	—	[55]
d-NVO@MXene	498 mAh/g at 0.5 A/g, 200 mAh/g at 5.0 A/g	75% capacity retention after 1000 cycles at 5.0 A/g	—	[48]
MnO_x/MXene	85.0 mAh/g at 0.1 A/g, 45 mAh/g at 10 A/g	Nearly 100% capacity retention after 400 cycles at 5.0 A/g	40 mAh/g at 10 A/g	[56]
MnO_2/MXene	301.2 mAh/g at 0.1 A/g, 202.2 mAh/g at 2.0 A/g	90.6% capacity retention after 2000 cycles at 0.5 A/g	275 mAh/g at 0.1 A/g	[57]
$ZnMn_2O_4$/MXene	175.0 mAh/g at 0.1 A/g, 84.5 mAh/g at 4.0 A/g	92.4% capacity retention after 5000 cycles at 1.0 A/g	126 mAh/g at 0.1 A/g	[58]
Tris(aza)pentacene/ MXene	303.0 mAh/g at 0.04 A/g, 148.0 mAh/g at 2.0 A/g	81.6% capacity retention after 10 000 cycles at 1.0 A/g	150 mAh/g at 1 A/g	[59]
Polyaniline/ MXene	262.0 mAh/g at 0.5 A/g, 160.0 mAh/g at 15 A/g	64.4% capacity retention after 5000 cycles at 15 A/g	188 mAh/g at 1 A/g	[60]

specific capacity of 388 mAh/g at a current density of 0.1 A/g and maintained a remarkable capacity of 212.1 mAh/g even if the current density increased to 10 A/g. After 3700 cycles at 3 A/g, the capacity retention remains close to 100%, demonstrating excellent cycling stability. More notably, TNVO11 retains a high capacity of 320.7 mAh/g at 0.1 A/g if used as a flexible battery electrode and successfully overcomes the limitations of flexible batteries under twisting conditions. At a current density of 1 A/g, the material can maintain stable high-capacity output even under bending and twisting conditions.

Data availability

All data needed to support the conclusions in the paper are presented in the manuscript. Additional data related to this paper may be requested from the corresponding author upon request.

Acknowledgements

This work was supported by the National Natural Science Foundation of China (Nos. 52372284, 52275187, and 52202364), Natural Science Foundation of Henan (No. 232300421135), and Henan Central-Guided Local S&T Development Fund (No. Z20241471061).

Declaration of competing interest

All the contributing authors report no conflict of interests in this work.

Author contribution statement

G. L. Z.: Writing – review & editing, writing – original draft, methodology, investigation, data curation. J. C. F.: Writing – original draft, methodology, investigation, data curation. J. L. G.: Investigation, data curation. X. L. Z.: Investigation, data curation. J. D. S.: Investigation. L. B. W.: Methodology, project administration. Y. K. C.: Formal analysis, methodology. A. G. Z.: Writing – review & editing, resources, project administration, conceptualization. All the authors have approved the final manuscript.

Use of AI statement

None.

References

[1] Zhao, Z. X.; He, Y.; Yu, W. T.; Shang, W. X.; Ma, Y. Y.; Tan, P. Revealing the missing puzzle piece of concentration in regulating Zn electrodeposition. *Proc. Natl. Acad. Sci. USA* **2023**, *120*, e2307847120.

[2] Blanc, L. E.; Kundu, D.; Nazar, L. F. Scientific challenges for the implementation of Zn-ion batteries. *Joule* **2020**, *4*, 771–799.

[3] Fang, L.; Lin, L.; Wu, Z. M.; Xu, T. H.; Wang, X. X.; Chang, L. M.; Nie, P. High-performance layered CaV_4O_9-MXene composite cathodes for aqueous zinc ion batteries. *Nanomaterials* **2023**, *13*, 1536.

[4] Li, M.; Li, X. L.; Qin, G. F.; Luo, K.; Lu, J.; Li, Y. B.; Liang, G. J.; Huang, Z. D.; Zhou, J.; Hultman, L. et al. Halogenated Ti_3C_2 MXenes with electrochemically active terminals for high-performance zinc ion batteries. *ACS Nano* **2021**, *15*, 1077–1085.

[5] Liu, Z. P.; Sun, B.; Zhang, Y.; Zhang, Q. X.; Fan, L. S. Polymer-adjusted zinc anode towards high-performance aqueous zinc ion batteries. *Prog. Polym. Sci.* **2024**, *152*, 101817.

[6] Wang, Q. H.; Zhao, J. Q.; Zhang, J.; Li, M.; Tan, F. P.; Xue, X. L.; Sui, Z. Y.; Zou, Y. F.; Zhang, X.; Zhang, W. et al. Biomass chitin nanofiber separators proactively stabilizing zinc anodes for dendrite-free aqueous zinc-ion batteries. *Adv. Funct. Mater.* **2024**, *34*,

2405957.
[7] Wu, Z. Y.; Ye, F.; Liu, Q.; Pang, R.; Liu, Y.; Jiang, L.; Tang, Z. L.; Hu, L. F. Simultaneous incorporation of V and Mn element into polyanionic NASICON for high energy-density and long-lifespan Zn-ion storage. *Adv. Energy Mater.* **2022**, *12*, 2200654.
[8] Li, Y.; Guo, Y. F.; Li, Z. X.; Wang, P. F.; Xie, Y.; Yi, T. F. Carbon-based nanomaterials for stabilizing zinc metal anodes towards high-performance aqueous zinc-ion batteries. *Energy Storage Mater.* **2024**, *67*, 103300.
[9] Li, G. J.; Sun, L.; Zhang, S. L.; Zhang, C. F.; Jin, H. Y.; Davey, K.; Liang, G. M.; Liu, S. L.; Mao, J. F.; Guo, Z. P. Developing cathode materials for aqueous zinc ion batteries: Challenges and practical prospects. *Adv. Funct. Mater.* **2023**, *34*, 2301291.
[10] Wu, Z. Y.; Lu, C. J.; Ye, F.; Zhang, L.; Jiang, L.; Liu, Q.; Dong, H. L.; Sun, Z. M.; Hu, L. F. Bilayered $VOPO_4{\cdot}2H_2O$ nanosheets with high-concentration oxygen vacancies for high-performance aqueous zinc-ion batteries. *Adv. Funct. Mater.* **2021**, *31*, 2106816.
[11] Liu, C. Z.; Xu, W. W.; Mei, C. T.; Li, M. C.; Xu, X. W.; Wu, Q. L. Highly stable $H_2V_3O_8$/MXene cathode for Zn-ion batteries with superior rate performance and long lifespan. *Chem. Eng. J.* **2021**, *405*, 126737.
[12] Yu, A.; Zhang, W.; Joshi, N.; Yang, Y. Recent advances in anode design for mild aqueous Zn-ion batteries. *Energy Storage Mater.* **2024**, *64*, 103075.
[13] Wan, F.; Zhang, L. L.; Dai, X.; Wang, X. Y.; Niu, Z. Q.; Chen, J. Aqueous rechargeable zinc/sodium vanadate batteries with enhanced performance from simultaneous insertion of dual carriers. *Nat. Commun.* **2018**, *9*, 1656.
[14] Zhao, J. X.; Lu, H. Y.; Peng, J. H.; Li, X. F.; Zhang, J. J.; Xu, B. G. Establishing aqueous zinc-ion batteries for sustainable energy storage. *Energy Storage Mater.* **2023**, *60*, 102846.
[15] Ding, Y.; Zhang, L. L.; Wang, X.; Han, L. N.; Zhang, W. K.; Guo, C. L. Vanadium-based cathodes for aqueous zinc ion batteries: Structure, mechanism and prospects. *Chin. Chem. Lett.* **2023**, *34*, 107399.
[16] Ma, L. J.; Wang, X. L.; Chen, X.; Gao, J. B.; Wang, Y. W.; Song, Y. H.; Zhao, Y. R.; Gao, S. Z.; Li, L.; Sun, J. C. Boosting the zinc storage performance of vanadium dioxide by integrated morphology engineering and carbon nanotube conductive networks. *Nano Res.* **2024**, *17*, 7136–7143.
[17] Liu, H. W.; Wang, N. Z.; Hu, L.; Sun, M. X.; Li, Z. J.; Jia, C. Y. Constructing graphene conductive networks in manganese vanadate as high-performance cathode for aqueous zinc-ion batteries. *Electrochim. Acta* **2023**, *441*, 141856.
[18] Zhang, N. N.; Huang, S.; Yuan, Z. S.; Zhu, J. C.; Zhao, Z. F.; Niu, Z. Q. Direct self-assembly of MXene on zn anodes for dendrite-free aqueous zinc-ion batteries. *Angew. Chem., Int. Ed.* **2021**, *60*, 2861–2865.
[19] Chang, Y. K.; Zhao, H. L.; Liu, X.; Huo, Y. J.; Dong, B. B.; Wang, L. B.; Bala, H.; Hu, Q. K.; Zhou, A. G. Etching-time-regulated strategy toward delaminated Mo_2CT_x MXene for tailoring electromagnetic wave absorption. *J. Adv. Ceram.* **2024**, *13*, 1795–1806.
[20] Bi, S. S.; Zhang, Y.; Deng, S. Z.; Tie, Z. W.; Niu, Z. Q. Proton-assisted aqueous manganese-ion battery chemistry. *Angew. Chem., Int. Ed.* **2022**, *61*, e202200809.
[21] He, P.; Yan, M. Y.; Zhang, G. B.; Sun, R. M.; Chen, L. N.; An, Q. Y.; Mai, L. Q. Layered VS_2 nanosheet-based aqueous Zn ion battery cathode. *Adv. Energy Mater.* **2017**, *7*, 1601920.
[22] Zhang, Y.; Zhang, G. C.; Ma, Z. L.; Qin, J. B.; Shen, X. Heterogeneous MXene-based films with graded electrical conductivity towards highly efficient EMI shielding and electrothermal heating. *Nano Res.* **2024**, *17*, 7264–7274.
[23] Jin, X. H.; Mo, D. J.; Feng, L. R.; Wang, D.; Su, B. L.; Guo, X. H. Amino-functionalized and Na^+ pre-intercalated three-dimensional $Ti_3C_2T_x$ film aerogel with excellent electrochemical performances for supercapacitor. *Nano Res.* **2025**, *18*, 94907092.
[24] Barsoum, M. W. The $M_{N+1}AX_N$ phases: A new class of solids. *Prog. Solid State Chem.* **2000**, *28*, 201–281.
[25] Gogotsi, Y.; Anasori, B. The rise of MXenes. *ACS Nano* **2019**, *13*, 8491–8494.
[26] Zhou, A. G.; Liu, Y.; Li, S. B.; Wang, X. H.; Ying, G. B.; Xia, Q. X.; Zhang, P. G. From structural ceramics to 2D materials with multi-applications: A review on the development from MAX phases to MXenes. *J. Adv. Ceram.* **2021**, *10*, 1194–1242.
[27] Zhang, G. L.; Du, Y. Q.; Hu, M. H.; Hu, Q. K.; Zhou, A. G. Spark plasma sintering of nove MAX phase Mo_2Ga_2C. *Adv. Ceram.* **2023**, *44*, 481–489.
[28] Geng, H. Q.; Li, X. M.; Gao, X. J.; Cong, Y. L.; Liu, Q.; Li, J. J.; Guan, Y.; Wang, L. M.; He, W. W. Highly adhesive and catalytic VO_xC nanosheets with strong antibacterial activity. *Nano Today* **2023**, *52*, 101989.
[29] Guo, Y. T.; Zhang, X.; Jin, S.; Xia, Q. X.; Chang, Y. K.; Wang, L. B.; Zhou, A. G. Synthesis of Mo_2C MXene with high electrochemical performance by alkali hydrothermal etching. *J. Adv. Ceram.* **2023**, *12*, 1889–1901.
[30] Naguib, M.; Kurtoglu, M.; Presser, V.; Lu, J.; Niu, J. J.; Heon, M.; Hultman, L.; Gogotsi, Y.; Barsoum, M. W. Two-dimensional nanocrystals produced by exfoliation of Ti_3AlC_2. *Adv. Mater.* **2011**, *23*, 4248–4253.
[31] Halim, J.; Kota, S.; Lukatskaya, M. R.; Naguib, M.; Zhao, M. Q.; Moon, E. J.; Pitock, J.; Nanda, J.; May, S. J.; Gogotsi, Y. et al. Synthesis and characterization of 2D molybdenum carbide (MXene). *Adv. Funct. Mater.* **2016**, *26*, 3118–3127.
[32] Ren, Y. P.; Zhou, X. L.; Gao, X. J.; Si, J. J.; Ren, W. H.; Li, C. X.; Yang, Q.; Zhou, Y. L.; Bai, F.; He, W. W. Ultra-high antioxidant, anti-apoptosis and pro-angiogenesis effect of Mo_2C nanosheets for treatment of diabetic wounds. *Nano Today* **2024**, *55*, 102202.
[33] Eom, W.; Shin, H.; Ambade, R. B.; Lee, S. H.; Lee, K. H.; Kang, D. J.; Han, T. H. Large-scale wet-spinning of highly electroconductive MXene fibers. *Nat. Commun.* **2020**, *11*, 2825.
[34] Liu, Q.; Ren, Y. P.; Jia, H. M.; Yuan, H.; Tong, Y. P.; Kotha, S.; Mao, X. B.; Huang, Y. W.; Chen, C. Y.; Zheng, Z. et al. Vanadium carbide nanosheets with broad-spectrum antioxidant activity for pulmonary fibrosis therapy. *ACS Nano* **2023**, *17*, 22527–22538.
[35] Park, J. M.; Jana, M.; Baek, S. H.; Kang, T.; Xiong, P. X.; Park, J. H.; Kim, J. S.; Zeraati, A. S.; Shekhirev, M.; Braun, P. V. et al. MXene ink hosting zinc anode for high performance aqueous zinc metal batteries. *J. Energy Chem.* **2023**, *76*, 187–194.
[36] Zhang, G. X.; Yang, H.; Zhou, H. J.; Huang, T. Y.; Yang, Y. F.; Zhu, G. Y.; Zhang, Y. Z.; Pang, H. MXene-mediated interfacial growth of 2D–2D heterostructured nanomaterials as cathodes for Zn-based aqueous batteries. *Angew. Chem., Int. Ed.* **2024**, *63*, e202401903.
[37] Wei, X. Y.; Xue, K. J.; Wei, Y. T.; Wang, S. M.; Zhang, X.; Wang, X. H.; Wang, Q. G. Two-dimensional copper vanadate intercalated vanadium carbide MXene nanoplates as a high-performance cathode for aqueous Zn-ion batteries. *Synth. Met.* **2024**, *305*, 117600.
[38] Wang, Q.; Wang, M. J.; Wen, L.; Zeng, W.; Ge, B. H.; Zhang, C. F.; Yue, Y.; Wang, S. L. A new (de)intercalation MXene/Bi cathode for ultrastable aqueous zinc-ion battery. *Adv. Funct. Mater.* **2024**, *34*, 2214506.
[39] Li, L.; Zhou, A. G.; Xu, L.; Li, Z. Y.; Wang, L. B. Synthesis of high pure Ti_3AlC_2 and Ti_2AlC powders from TiH_2 powders as Ti source by tube furnace. *J. Wuhan Univ. Technol. Mat. Sci. Ed.* **2013**, *28*, 882–887.
[40] Wu, M.; An, Y. P.; Yang, R.; Tao, Z. H.; Xia, Q. X.; Hu, Q. K.; Li, M.; Chen, K.; Zhang, Z. Y.; Huang, Q. et al. V_2CT_x and $Ti_3C_2T_x$ MXenes nanosheets for gas sensing. *ACS Appl. Nano Mater.* **2021**, *4*, 6257–6268.
[41] Jin, S.; Su, T. C.; Hu, Q. K.; Zhou, A. G. Thermal conductivity and electrical transport properties of double-A-layer MAX phase Mo_2Ga_2C. *Mater. Res. Lett.* **2020**, *8*, 158–164.
[42] Guo, Y. T.; Jin, S.; Wang, L. B.; He, P. G.; Hu, Q. K.; Fan, L. Z.; Zhou, A. G. Synthesis of two-dimensional carbide Mo_2CT_x MXene by hydrothermal etching with fluorides and its thermal stability. *Ceram.*

Int. **2020**, *46*, 19550–19556.
[43] He, H. T.; Jin, S.; Fan, G. X.; Wang, L. B.; Hu, Q. K.; Zhou, A. G. Synthesis mechanisms and thermal stability of ternary carbide Mo_2Ga_2C. *Ceram. Int.* **2018**, *44*, 22289–22296.
[44] Jin, S.; Guo, Y. T.; Wang, J. K.; Wang, L. B.; Hu, Q. K.; Zhou, A. G. Carbon dioxide adsorption of two-dimensional Mo_2C MXene. *Diam. Relat. Mater.* **2022**, *128*, 109277.
[45] Halim, J.; Cook, K. M.; Naguib, M.; Eklund, P.; Gogotsi, Y.; Rosen, J.; Barsoum, M. W. X-ray photoelectron spectroscopy of select multi-layered transition metal carbides (MXenes). *Appl. Surf. Sci.* **2016**, *362*, 406–417.
[46] Jin, S.; Jing, H. J.; Wang, L. B.; Hu, Q. K.; Zhou, A. G. Mo_2C MXene nanosheets made in different etching solutions as co-catalysts for hydrogen production. *ACS Appl. Nano Mater.* **2023**, *6*, 9746–9756.
[47] Li, X. J.; Zhu, X. D.; Cao, Z. Y.; Xu, Z. L.; Shen, J. F.; Ye, M. X. *In situ* electrochemical transformation toward structure optimized VEG@MXene cathode for enhanced zinc-ion storage. *Small* **2022**, *18*, 2105325.
[48] Qi, J. J.; Zhang, Y. F.; Wen, J. J.; Zhai, H. N.; Li, M.; Zhang, Y. N.; Xu, H. T.; Yang, W. Y.; Li, C. L.; Wang, H. H. et al. Freestanding defective ammonium vanadate@MXene hybrid films cathode for high performance aqueous zinc ion batteries. *J. Colloid Interface Sci.* **2023**, *652*, 285–293.
[49] Jia, R.; Yin, C. J.; Wang, B.; Li, L.; Hu, J. S. Polyaniline-coated sodium vanadate nanorods cathode boosting zinc ion dynamics in aqueous zinc-ion batteries. *Chem. Eng. J.* **2024**, *500*, 157587.
[50] Bi, W. C.; Gao, G. H.; Wu, G. M.; Atif, M.; AlSalhi, M.; Cao, G. Z. Sodium vanadate/PEDOT nanocables rich with oxygen vacancies for high energy conversion efficiency zinc ion batteries. *Energy Storage Mater.* **2021**, *40*, 209–218.
[51] Liu, Y.; Lu, C. J.; Yang, Y. T.; Chen, W. S.; Ye, F.; Dong, H. L.; Wu, Y. P.; Ma, R. Z.; Hu, L. F. Multiple cations nanoconfinement in ultrathin V_2O_5 nanosheets enables ultrafast ion diffusion kinetics toward high-performance zinc ion battery. *Adv. Mater.* **2024**, *36*, 2312982.
[52] Wang, Y. L.; Liu, L. W.; Wang, Y. P.; Qu, J. L.; Chen, Y.; Song, J. Atomically coupled 2D MnO_2/MXene superlattices for ultrastable and fast aqueous zinc-ion batteries. *ACS Nano* **2023**, *17*, 21761–21770.
[53] Guan, J. D.; Shao, L. Y.; Yu, L.; Wang, S. G.; Shi, X. Y.; Cai, J. J.; Sun, Z. P. Two-dimensional $Mg_{0.2}V_2O_5{\cdot}nH_2O$ nanobelts derived from V_4C_3 MXenes for highly stable aqueous zinc ion batteries. *Chem. Eng. J.* **2022**, *443*, 136502.
[54] Xu, Z. B.; Li, X. L.; Jin, Y. A.; Dong, Q.; Ye, J. J.; Zhang, X. Q.; Qian, Y. T. Monodispersed flower-like MXene@VO_2 clusters for aqueous zinc ion batteries with superior rate performance. *Nanoscale* **2022**, *14*, 11655–11663.
[55] Cai, S. N.; Wu, Y. K.; Chen, H.; Ma, Y. D.; Fan, T. X.; Xu, M. W.; Bao, S. J. Why does the capacity of vanadium selenide based aqueous zinc ion batteries continue to increase during long cycles? *J. Colloid Interface Sci.* **2022**, *615*, 30–37.
[56] Luo, S. J.; Xie, L. Y.; Han, F.; Wei, W.; Huang, Y.; Zhang, H.; Zhu, M. S.; Schmidt, O. G.; Wang, L. Nanoscale parallel circuitry based on interpenetrating conductive assembly for flexible and high-power zinc ion battery. *Adv. Funct. Mater.* **2019**, *29*, 1901336.
[57] Shi, M. J.; Wang, B.; Chen, C.; Lang, J. W.; Yan, C.; Yan, X. B. 3D high-density MXene@MnO_2 microflowers for advanced aqueous zinc-ion batteries. *J. Mater. Chem. A* **2020**, *8*, 24635–24644.
[58] Shi, M. J.; Wang, B.; Shen, Y.; Jiang, J. T.; Zhu, W. H.; Su, Y. J.; Narayanasamy, M.; Angaiah, S.; Yan, C.; Peng, Q. 3D assembly of MXene-stabilized spinel $ZnMn_2O_4$ for highly durable aqueous zinc-ion batteries. *Chem. Eng. J.* **2020**, *399*, 125627.
[59] Wang, X. S.; Liu, Y. N.; Wei, Z. Y.; Hong, J. Z.; Liang, H. B.; Song, M. X.; Zhou, Y.; Huang, X. X. MXene-boosted imine cathodes with extended conjugated structure for aqueous zinc-ion batteries. *Adv. Mater.* **2022**, *34*, 2206812.
[60] Liu, Y.; Dai, Z. W.; Zhang, W.; Jiang, Y.; Peng, J.; Wu, D. L.; Chen, B.; Wei, W.; Chen, X.; Liu, Z. J. et al. Sulfonic-group-grafted $Ti_3C_2T_x$ MXene: A silver bullet to settle the instability of polyaniline toward high-performance Zn-ion batteries. *ACS Nano* **2021**, *15*, 9065–9075.